Configuration Tracking for Soft Continuum Robotic Arms Using Inverse Dynamic Control of a Cosserat Rod Model

Azadeh Doroudchi and Spring Berman

***Abstract*— Controlling the configuration of a soft continuum robot arm is challenging due to the hyper-redundant kinematics of such robots. We propose a new model-based, inverse dynamic control approach to this problem that is defined on the configuration state variables of the geometrically exact Cosserat rod model. Our approach is capable of controlling a soft continuum robot to track static or time-varying 3D configurations through bending, torsion, shear, and extension deformations. The controller has a decentralized structure, in which the gain matrices can be defined in terms of the physical and material properties of distinct cross-sections of the robot arm. This structure facilitates its implementation on continuum robot arms composed of independently-controllable segments that have local sensing and actuation. The controller is validated with numerical simulations in MATLAB with a hydrogel-based soft robot arm that can produce the four primary types of deformations. The simulated arm successfully tracks these configurations with average normalized root-mean-square errors (NRMSE) below 7% in all cases. To demonstrate the generality of the control approach, its performance is also validated on a larger simulated robot arm made of silicone.**

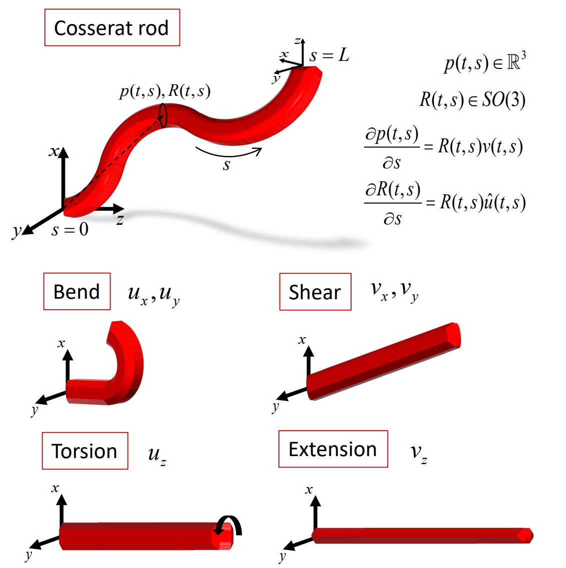

Fig. 1. Schematic of a Cosserat rod. The equations for the 3-dimensional rod configuration describe the relationships between the curvature vector ($\boldsymbol{u}$), the rate of change of position with respect to arc length ($\boldsymbol{v}$), and the resulting bending, torsion, shear, and extension deformations.

I. Introduction

Soft continuum robots are fabricated from soft materials [1] and designed with a continuous backbone [2]. Due to their hyper-redundant kinematics, these robots have high dexterity (infinite degrees of freedom) and compliance, with the ability to grasp objects and perform manipulation tasks that rigid-link robots cannot [3]. Soft robot arms are usually actuated with tendon, cable, pneumatic, or hydraulic actuators [4]. Over the past decade, local actuation for soft robots has advanced [5], [6], [7]. For example, [8] introduces an independently-controllable local actuation unit made of temperature-responsive hydrogel, called an SVA (Soft Voxel Actuator), that we used to fabricate a soft robot arm with distributed actuation in our prior work [9]. The development of local actuators can be distributed through a soft robot enables the implementation of decentralized control approaches on such robots, which would display robust performance to individual actuator failures. Decentralized control approaches, in general, can be used to overcome limitations of centralized control approaches when applied to large-scale systems, such as high computational complexity, delays, uncertainties, and a lack of robustness [10].

This work was supported by Office of Naval Research (ONR) Award N00014-17-1-2117.

A. Doroudchi is with the School of Electrical, Computer and Energy Engineering, Arizona State University (ASU), Tempe, AZ, 85287 {adoroudc}@asu.edu. S. Berman is with the School for Engineering of Matter, Transport and Energy, ASU, Tempe, AZ, 85287 {spring.berman}@asu.edu.

Continuum robots are inspired by soft-bodied animals and muscular hydrostats such as octopuses, snakes, elephant trunks, worms, and animal tongues [11], [12]. Octopuses in particular have been a rich source of inspiration for roboticists [6], due in part to the dexterity and flexibility of their continuously deformable arms that are capable of four primary deformations: bending, twisting, shortening, and elongation [13]. In previous studies, only one or two of these four types of deformations were simulated or experimentally produced in a soft continuum robot, depending on the control objective or model limitations [14], [15], [16]. In this paper, we present a new approach to dynamic control of a soft continuum robot arm that enables the arm to track reference configurations which require all four primary deformations. This control approach is decentralized, and it can be used to reshape such robots into complex configurations for a wide range of tasks.

Geometrically exact models using Cosserat rod theory have been widely applied to static and dynamic modeling of soft continuum robots, as they are able to accurately represent large deformations from bending, torsion, shear, and extension [17]. The Kirchhoff model, a special case of the Cosserat model, can only describe bending and torsion movements; in other words, it is an unshearable and inextensible Cosserat rod model [18]. In [9], we used the numerical forward solution of the Cosserat rod model presented in [18] to experimentally demonstrate open-loop control of bending deformation in our hydrogel SVA-actuated soft robot arm. The piecewise constant strain (PCS) model is a continuous Cosserat model that describes shear and torsion [19]. Other common dynamic modeling approaches are based on the classic Lagrangian or Newton-Euler formulations for rigid-link robots [20].

The majority of static and dynamic controllers for continuum robots use the standard Lagrangian formulation for modeling the robot and the Jacobian formulation for closed-loop real-time inverse dynamic control [21], [22], [7], [23], [24]. In [21], a closed-loop control approach for trajectory tracking and surface following using the inverse dynamics of the Lagrangian formulation was implemented experimentally in 2D for the first time on a pneumatically actuated soft robotic arm. A few real-time control approaches based on reduced-order finite element methods have been developed and tested on soft robots and manipulators using the Simulation Open Framework Architecture (SOFA) software framework [25], [26]. To address the lack of control methodologies that take full advantage of body compliance, a compliant mechanics environment for controlling soft robots was presented in [27] that uses the recently developed software package Elastica, an open-source simulation environment for slender rods that can bend, twist, shear, and stretch. Other studies from this group [28], [29] propose methods for controlling an octopus-inspired soft arm with muscle-like actuation.

In this paper, we develop a novel decentralized control approach for configuration tracking by soft continuum robot arms composed of independently-controllable segments with with local sensing and actuation. This control approach enables such robots to track 3D configurations that involve any combination of bending, torsion, shear, and extension deformations. The approach can be implemented on continuum robots with dynamics that can be described by the geometrically exact Cosserat rod model. We validate our control approach in numerical simulations of both hydrogel-based and silicone continuum robot arms.

II. Forward Dynamics of a Cosserat Rod Model

We aim to develop a model of the nonlinear dynamics of an octopus-inspired soft continuum robot arm that accounts for the effects of large deformations due to bending, torsion, shear, and extension [17]. A suitable candidate is the Cosserat rod model, for which three assumptions are required: a sufficiently large length-to-diameter ratio, material incompressability, and linear elasticity [17].

Figure 1 depicts a 3-dimensional uniform Cosserat rod in Cartesian coordinates. The length of the rod is denoted by L, the density of the rod by ρ, and the area and second mass moment of inertia tensor of each cross-section by A and $\boldsymbol{J}$, respectively. The position and orientation matrix of each cross-section at arc length s in the global coordinate frame are denoted by ${}^{G}\boldsymbol{p}(t,s) \in \mathbb{R}^3$ and ${}^{G}\boldsymbol{R}(t,s) \in SO(3)$, respectively. From this point on, whenever a variable does not have the global frame annotation G, it means that it is defined with respect to a local coordinate frame that is fixed to the cross-section in which the variable is defined. In the Cosserat dynamics of a rod whose neutral axis is in the z direction, the curvature vector $\boldsymbol{u}(t,s) = [\boldsymbol{u}_x, \boldsymbol{u}_y, \boldsymbol{u}_z]^T$ and the rate of change of position $\boldsymbol{v}(t,s) = [\boldsymbol{v}_x, \boldsymbol{v}_y, \boldsymbol{v}_z]^T$ are directly responsible for deformations of the rod, and we will refer to them as configuration state variables. The vectors $\boldsymbol{u}_x$ and $\boldsymbol{u}_y$ produce bending about the x and y axes, and $\boldsymbol{u}_z$ creates torsion about the z-axis. The vectors $\boldsymbol{v}_x$ and $\boldsymbol{v}_y$ cause shear effects that produce changes in the size of the cross-section, and $\boldsymbol{v}_z$ produces extension along the z-axis. The vectors $\boldsymbol{q}(t,s)$ and $\boldsymbol{w}(t,s)$ define velocity and angular velocity. The internal force and moment are represented by ${}^{G}\boldsymbol{n}(t,s) \in \mathbb{R}^3$ and ${}^{G}\boldsymbol{m}(t,s) \in \mathbb{R}^3$, respectively. They are the force and moment that the material at $\boldsymbol{p}(t, s+ds)$ exerts on the material at $\boldsymbol{p}(t, s-ds)$, for infinitesimal ds.

A set of partial differential equations, differentiated with respect to arc length s and time t, governs the deformation of each cross-section along the elastic Cosserat rod (Fig. 1). The spatial derivatives of the state variables are calculated at each cross-section of the rod. The internal force and moment evolve according to the equations:

$$\begin{aligned} {}^{G}\boldsymbol{n}_s &= {}^{G}\boldsymbol{R}\rho A(\widehat{\boldsymbol{w}}\boldsymbol{q} + \boldsymbol{q}_t) - {}^{G}\boldsymbol{f}, \\ {}^{G}\boldsymbol{m}_s &= {}^{G}\boldsymbol{R}\rho(\widehat{\boldsymbol{w}}\boldsymbol{J}\boldsymbol{w} + \boldsymbol{J}\boldsymbol{w}_t) - {}^{G}\widehat{\boldsymbol{p}}_s {}^{G}\boldsymbol{n} - {}^{G}\boldsymbol{l}, \end{aligned} \tag{1}$$

and the kinematic variables evolve according to:

$$\begin{aligned} {}^{G}\boldsymbol{p}_s &= {}^{G}\boldsymbol{R}\boldsymbol{v}\ , {}^{G}\boldsymbol{p}_t = \boldsymbol{R}\boldsymbol{q}, \\ {}^{G}\boldsymbol{R}_s &= {}^{G}\boldsymbol{R}\widehat{\boldsymbol{u}}\ , {}^{G}\boldsymbol{R}_t = \boldsymbol{R}\widehat{\boldsymbol{w}}, \\ \boldsymbol{q}_s &= \boldsymbol{v}_t - \widehat{\boldsymbol{u}}\boldsymbol{q} + \widehat{\boldsymbol{w}}\boldsymbol{v}, \\ \boldsymbol{w}_s &= \boldsymbol{u}_t - \widehat{\boldsymbol{u}}\boldsymbol{w}, \end{aligned} \tag{2}$$

where $\widehat{(\cdot)}$ is the cross product matrix of a vector. The time derivatives are computed using the Backward Differentiation Formula (BDF) [30], [31] as follows:

$$\begin{aligned} \boldsymbol{v}_t &= c_0\boldsymbol{v}^i + \boldsymbol{v}_h, \quad \boldsymbol{v}_h = c_1\boldsymbol{v}^{i-1} + c_2\boldsymbol{v}^{i-2}, \\ \boldsymbol{u}_t &= c_0\boldsymbol{u}^i + \boldsymbol{u}_h, \quad \boldsymbol{u}_h = c_1\boldsymbol{u}^{i-1} + c_2\boldsymbol{u}^{i-2}, \\ \boldsymbol{q}_t &= c_0\boldsymbol{q}^i + \boldsymbol{q}_h, \quad \boldsymbol{q}_h = c_1\boldsymbol{q}^{i-1} + c_2\boldsymbol{q}^{i-2}, \\ \boldsymbol{w}_t &= c_0\boldsymbol{w}^i + \boldsymbol{w}_h, \quad \boldsymbol{w}_h = c_1\boldsymbol{w}^{i-1} + c_2\boldsymbol{w}^{i-2}, \end{aligned} \tag{3}$$

in which $c_0 = 1.5/dt$, $c_1 = -2/dt$, and $c_2 = 0.5/dt$ are the implicit difference coefficients. The elements $(\cdot)^{(i)}$ are the values of the corresponding variables at time step i, and the history elements, $(\cdot)_h$, are the values of the corresponding variables at the two previous time steps, $i-1$ and $i-2$.

The equations of an elastic Cosserat rod are written for its central backbone, and any forces and moments that are applied to this backbone are modeled as external forces and moments, denoted by ${}^{G}\boldsymbol{f}$ and ${}^{G}\boldsymbol{l}$, respectively. In practice, these forces and moments are the sum of the control inputs applied by the actuators of the continuum robot arm (${}^{G}\boldsymbol{f}_a, {}^{G}\boldsymbol{l}_a$), external loads on the arm (${}^{G}\boldsymbol{f}_l, {}^{G}\boldsymbol{l}_l$), and environmental effects (${}^{G}\boldsymbol{f}_e, {}^{G}\boldsymbol{l}_e$):

$$\begin{aligned} {}^{G}\boldsymbol{f} &= {}^{G}\boldsymbol{f}_a + {}^{G}\boldsymbol{f}_l + {}^{G}\boldsymbol{f}_e, \\ {}^{G}\boldsymbol{l} &= {}^{G}\boldsymbol{l}_a + {}^{G}\boldsymbol{l}_l + {}^{G}\boldsymbol{l}_e. \end{aligned} \tag{4}$$

Our approach to numerically solving (1) is outlined in Algorithm 1. The implicit fourth-order Runge-Kutta (RK4) method is implemented to numerically integrate (1) with respect to space, and then the standard shooting method (SSM) is used to generate initial guesses $\boldsymbol{n}_0, \boldsymbol{m}_0$ of $\boldsymbol{n}, \boldsymbol{m}$ at each time step. The following boundary conditions of the fixed end of the rod are known:

$$\begin{aligned} {}^G\boldsymbol{p}(t,0) = \boldsymbol{p}_0, \ {}^G\boldsymbol{R}(t,0) = \boldsymbol{R}_0, \\ \boldsymbol{q}(t,0) = 0, \quad \boldsymbol{w}(t,0) = 0. \end{aligned} \tag{5}$$

The SSM guesses the following unknown boundary conditions of the fixed end of the rod,

$${}^G\boldsymbol{n}(t,0) = \boldsymbol{n}_0, \quad {}^G\boldsymbol{m}(t,0) = \boldsymbol{m}_0, \tag{6}$$

while satisfying the known boundary conditions of the free end,

$${}^G\boldsymbol{n}(t,L) = \boldsymbol{n}_L = \boldsymbol{0}, \quad {}^G\boldsymbol{m}(t,L) = \boldsymbol{m}_L = \boldsymbol{0}. \tag{7}$$

This two-point Boundary Value Problem (BVP) [30], [32], [33], which has been reduced to an Initial Value Problem (IVP), is solved by the SSM guesses at each iteration of Algorithm 1. Then, the guessed values are corrected by the Levenberg-Marquardt nonlinear optimization algorithm. A unique solution to the BVT is ensured by using a sufficiently small time step and using the solution at the previous time step as the initial guess for the current time step [34]. Then, the configuration state variables, $\boldsymbol{v}$ and $\boldsymbol{u}$, are found from the computed ${}^G\boldsymbol{n}$ and ${}^G\boldsymbol{m}$ as follows:

$$\begin{aligned} \boldsymbol{v} &= (\boldsymbol{K}_{se} + c_0\boldsymbol{B}_{se})^{-1}[{}^G\boldsymbol{R}^T \ {}^G\boldsymbol{n} + \boldsymbol{K}_{se}\boldsymbol{v}^* - \boldsymbol{B}_{se}\boldsymbol{v}_h], \\ \boldsymbol{u} &= (\boldsymbol{K}_{bt} + c_0\boldsymbol{B}_{bt})^{-1}[{}^G\boldsymbol{R}^T \ {}^G\boldsymbol{m} + \boldsymbol{K}_{bt}\boldsymbol{u}^* - \boldsymbol{B}_{bt}\boldsymbol{u}_h]. \end{aligned} \tag{8}$$

The vectors $\boldsymbol{v}^*$ and $\boldsymbol{u}^*$ are the values of $\boldsymbol{v}$ and $\boldsymbol{u}$ at the undeformed reference shape. The effects of shear and extension are characterized by $\boldsymbol{K}_{se}$ and the effects of bending and torsion by $\boldsymbol{K}_{bt}$, under the assumption that the continuum robot arm is slender, symmetric, homogeneous, and isotropic:

$$\boldsymbol{K}_{se} = \begin{bmatrix} \alpha_c G & 0 & 0 \\ 0 & \alpha_c G & 0 \\ 0 & 0 & E \end{bmatrix} A, \quad \boldsymbol{K}_{bt} = \begin{bmatrix} E & 0 & 0 \\ 0 & E & 0 \\ 0 & 0 & G \end{bmatrix} \boldsymbol{J}. \tag{9}$$

In these equations, G and E are the shear modulus and Young's modulus, respectively, and α_c is a constant which is equal to 4/3 for circular cross-sections and 3/2 for rectangular ones. The damping matrices $\boldsymbol{B}_{se} = \tau\boldsymbol{K}_{se}$ and $\boldsymbol{B}_{bt} = \tau\boldsymbol{K}_{bt}$ in Eq. (8) can be calculated from vibration tests [35], in which τ is twice the period of vibrations exhibited by the continuum robot arm's tip.

III. A Decentralized Approach to Inverse Dynamic Control

We design a controller with a decentralized structure that has distinct proportional-derivative (PD) gains at each location along the arc length of the Cosserat rod. For segmented soft continuum robots, this enables the independent control of each segment in a computationally efficient manner. We have previously developed decentralized control approaches for segmented soft robot arms with objectives of vibration dampening using H_∞ state feedback control [36] and trajectory tracking using a consensus-based method [37]. Here, a desired reference configuration is tracked ($\bar{\boldsymbol{v}}$, $\bar{\boldsymbol{u}}$), which may be static or time-varying and results in bending, twisting, shear, extension, or a combination of these deformations in 3D space. In another study [38], we developed a kinematic controller for trajectory tracking by the tip of a segmented hyper-redundant robot arm, modeled as a series of Gough-Stewart platforms, that is capable of producing all four deformations considered here. In both [38] and this paper, we consider robot arms that are comprised of a series of physically connected segments with local sensing and actuation, and both control approaches rely on calculations by a central computational unit. However, we use a kinematic model of the robot in [38] and a Cosserat-based dynamic model in this paper, and the robot's segments in [38] are assumed to exchange information with adjacent segments, which is not assumed here. Moreover, the control approach developed in [38] is centralized, whereas the approach presented here is decentralized.

The control law is defined to track a reference configuration ($\bar{\boldsymbol{v}}$, $\bar{\boldsymbol{u}}$) and to compensate for external loads and environmental effects. The control inputs below are applied by the actuators of the continuum robot arm to the backbone of the robot:

$$\begin{aligned} {}^G\boldsymbol{f}_a =& {}^G\boldsymbol{R}[\boldsymbol{K}_{m_1}\bar{\boldsymbol{v}}_{tt} + \boldsymbol{K}_{v_1}(\bar{\boldsymbol{v}}_t - \boldsymbol{v}_t) + \boldsymbol{K}_{p_1}(\bar{\boldsymbol{v}} - \boldsymbol{v})] \\ & - {}^G\boldsymbol{f}_l - {}^G\boldsymbol{f}_e, \\ {}^G\boldsymbol{l}_a =& {}^G\boldsymbol{R}[\boldsymbol{K}_{m_2}\bar{\boldsymbol{u}}_{tt} + \boldsymbol{K}_{v_2}(\bar{\boldsymbol{u}}_t - \boldsymbol{u}_t) + \boldsymbol{K}_{p_2}(\bar{\boldsymbol{u}} - \boldsymbol{u})] \\ & - {}^G\boldsymbol{l}_l - {}^G\boldsymbol{l}_e, \end{aligned} \tag{10}$$

where $\boldsymbol{K}_{m_1}, \boldsymbol{K}_{m_2}$ are 3×3 diagonal matrices whose diagonal entries are proportional to $\rho A, \rho\boldsymbol{J}$, respectively, and $\boldsymbol{K}_{v_1}, \boldsymbol{K}_{v_2}, \boldsymbol{K}_{p_1}, \boldsymbol{K}_{p_2}$ are gain matrices defined as:

$$\begin{aligned} \boldsymbol{K}_{v_1} = v_1\boldsymbol{B}_{se}, \quad \boldsymbol{K}_{p_1} = p_1\boldsymbol{K}_{se}, \\ \boldsymbol{K}_{v_2} = v_2\boldsymbol{B}_{bt}, \quad \boldsymbol{K}_{p_2} = p_2\boldsymbol{K}_{bt}, \end{aligned} \tag{11}$$

where we set the scalar coefficients to $v_1 = p_1 = p_2 = v_2 = 1$. In this way, the controller gains at a specific cross-section of the robot can be defined in terms of the physical properties (A, $\boldsymbol{J}$) of that cross-section, independently of the composition of other cross-sections. This facilitates its implementation on a segmented continuum robot arm with a decentralized control structure.

Algorithm 1 briefly describes our implementation of this configuration tracking controller. First, the desired configuration is defined in terms of the variables $\bar{\boldsymbol{v}}$ and $\bar{\boldsymbol{u}}$ (line 1). We define an *outer loop* that iterates over time steps (lines 2 to 10) and an *inner loop* that iterates over discretized spatial locations (nodes) along the backbone of the robot (lines 4 to 9). In the outer loop, the initial boundary condition values of $\boldsymbol{n}_0$ and $\boldsymbol{m}_0$ are guessed using SSM; in the first iteration, they are set to zero (line 3). By applying RK4 to (${}^G\boldsymbol{n}_{j-1}, {}^G\boldsymbol{m}_{j-1}$) and the derivatives of the internal force

Algorithm 1: Configuration tracking controller

1: Given a desired configuration $\bar{\boldsymbol{v}}, \bar{\boldsymbol{u}}$
2: **for** $i \leftarrow 0$ to T/dt **do**
3: $\quad \boldsymbol{n}_0^i, \boldsymbol{m}_0^i \leftarrow$ SSM ($\boldsymbol{n}_L^i = 0, \boldsymbol{m}_L^i = 0$)
4: $\quad$ **for** $j \leftarrow 0$ to L/ds **do**
5: $\qquad \boldsymbol{n}_j^i, \boldsymbol{m}_j^i \leftarrow$ RK4 ($\boldsymbol{n}_{j-1}^i, \boldsymbol{n}_{s,j}^i$) and ($\boldsymbol{m}_{j-1}^i, \boldsymbol{m}_{s,j}^i$)
6: $\qquad \boldsymbol{v}_j^i, \boldsymbol{u}_j^i \leftarrow \boldsymbol{n}_j^i, \boldsymbol{m}_j^i$, Forward dynamics (8)
7: $\qquad \boldsymbol{f}_{a,j}^i, \boldsymbol{l}_{a,j}^i \leftarrow$ Control law (10)
8: $\qquad \boldsymbol{n}_{s,j}^i, \boldsymbol{m}_{s,j}^i \leftarrow$ Substitute (4) in (1)
9: $\quad$ **end for**
10: **end for**

Note: $(\boldsymbol{n}, \boldsymbol{m}, \boldsymbol{f}, \boldsymbol{l})$ are defined in the global frame, and $(\boldsymbol{v}, \boldsymbol{u})$ in the local frame.

and moment with respect to arc length, their values at the current spatial node on the backbone, j, are computed (lines 5). After implementing the current internal force and moments in (8), the values for $\boldsymbol{v}_j$ and $\boldsymbol{u}_j$ are found (line 6). Then, using the error between the configuration variables and their desired values, the control law calculates the force and moment (${}^G\boldsymbol{f}_a$,${}^G\boldsymbol{l}_a$) that the actuators must apply to the corresponding backbone section (line 7), and then ${}^G\boldsymbol{n}_s$ and ${}^G\boldsymbol{m}_s$ are found for the next spatial node on the backbone (line 8). To demonstrate that the configuration tracking error converges to zero under this controller, first the closed-loop system dynamics are derived. By rearranging the equations in (1), we obtain:

$$\begin{aligned} {}^G\boldsymbol{f} &= {}^G\boldsymbol{R}\rho A(\widehat{\boldsymbol{w}}\boldsymbol{q} + \boldsymbol{q}_t) - {}^G\boldsymbol{n}_s, \\ {}^G\boldsymbol{l} &= {}^G\boldsymbol{R}\rho(\widehat{\boldsymbol{w}}\boldsymbol{J}\boldsymbol{w} + \boldsymbol{J}\boldsymbol{w}_t) - {}^G\widehat{\boldsymbol{p}}_s{}^G\boldsymbol{n} - {}^G\boldsymbol{m}_s. \end{aligned} \tag{12}$$

Then, by substituting in the sum of external forces and moments from (4) and keeping the actuator control inputs on the left-hand side, we obtain:

$$\begin{aligned} {}^G\boldsymbol{f}_a &= {}^G\boldsymbol{R}\rho A(\widehat{\boldsymbol{w}}\boldsymbol{q} + \boldsymbol{q}_t) - {}^G\boldsymbol{n}_s - {}^G\boldsymbol{f}_l - {}^G\boldsymbol{f}_e, \\ {}^G\boldsymbol{l}_a &= {}^G\boldsymbol{R}\rho(\widehat{\boldsymbol{w}}\boldsymbol{J}\boldsymbol{w} + \boldsymbol{J}\boldsymbol{w}_t) - {}^G\widehat{\boldsymbol{p}}_s{}^G\boldsymbol{n} - {}^G\boldsymbol{m}_s - {}^G\boldsymbol{l}_l - {}^G\boldsymbol{l}_e. \end{aligned} \tag{13}$$

Replacing ${}^G\boldsymbol{f}_a$ and ${}^G\boldsymbol{l}_a$ in (13) with the control law (10), the external loads and environmental forces and moments from both sides of the equations cancel out:

$$\begin{aligned} &{}^G\boldsymbol{R}[\boldsymbol{K}_{m_1}\bar{\boldsymbol{v}}_{tt} + \boldsymbol{K}_{v_1}(\bar{\boldsymbol{v}}_t - \boldsymbol{v}_t) + \boldsymbol{K}_{p_1}(\bar{\boldsymbol{v}} - \boldsymbol{v})] \\ &= {}^G\boldsymbol{R}\rho A(\widehat{\boldsymbol{w}}\boldsymbol{q} + \boldsymbol{q}_t) - {}^G\boldsymbol{n}_s, \\ &{}^G\boldsymbol{R}[\boldsymbol{K}_{m_2}\bar{\boldsymbol{u}}_{tt} + \boldsymbol{K}_{v_2}(\bar{\boldsymbol{u}}_t - \boldsymbol{u}_t) + \boldsymbol{K}_{p_2}(\bar{\boldsymbol{u}} - \boldsymbol{u})] \\ &= {}^G\boldsymbol{R}\rho(\widehat{\boldsymbol{w}}\boldsymbol{J}\boldsymbol{w} + \boldsymbol{J}\boldsymbol{w}_t) - {}^G\widehat{\boldsymbol{p}}_s{}^G\boldsymbol{n} - {}^G\boldsymbol{m}_s. \end{aligned} \tag{14}$$

The right-hand sides of these equations are the sums of the internal forces and moments with respect to the arc length. By defining $\boldsymbol{n'}_s$ and $\boldsymbol{m'}_s$ as the following expressions,

$$\begin{aligned} {}^G\boldsymbol{n'}_s &= {}^G\boldsymbol{R}\rho A(\widehat{\boldsymbol{w}}\boldsymbol{q} + \boldsymbol{q}_t) - {}^G\boldsymbol{n}_s, \\ {}^G\boldsymbol{m'}_s &= {}^G\boldsymbol{R}\rho(\widehat{\boldsymbol{w}}\boldsymbol{J}\boldsymbol{w} + \boldsymbol{J}\boldsymbol{w}_t) - {}^G\widehat{\boldsymbol{p}}_s{}^G\boldsymbol{n} - {}^G\boldsymbol{m}_s, \end{aligned} \tag{15}$$

and rewriting them in terms of the second time derivatives

TABLE I

PARAMETERS IN THE NUMERICAL SIMULATIONS.

Param.	Description	Value
ds	Spatial discretization (m)	L/N
dt	Time step (s)	0.1
N	Number of spatial nodes	80
N_v	Number of virtual segments	8
r_p	Undeformed radius of proximal segment (mm)	3
r_d	Undeformed radius of distal segment (mm)	0.5
L	Undeformed length of the hydrogel robot arm (mm)	45
ρ	Density of hydrogel actuator [40] (kg/m^3)	1300
E	Young's modulus of hydrogel actuator (MPa)	0.6
ρ_S	Density of silicone (kg/m^3)	2330
E_S	Young's modulus of silicone (GPa)	188

of the configuration state variables,

$$\begin{aligned} {}^G\boldsymbol{n'}_s &= {}^G\boldsymbol{R}\boldsymbol{K}_{m_1}\boldsymbol{v}_{tt}, \\ {}^G\boldsymbol{m'}_s &= {}^G\boldsymbol{R}\boldsymbol{K}_{m_2}\boldsymbol{u}_{tt}, \end{aligned} \tag{16}$$

the closed-loop configuration dynamics of the robot can be expressed in the following form:

$$\begin{aligned} \boldsymbol{K}_{m_1}\bar{\boldsymbol{v}}_{tt} + \boldsymbol{K}_{v_1}(\bar{\boldsymbol{v}}_t - \boldsymbol{v}_t) + \boldsymbol{K}_{p_1}(\bar{\boldsymbol{v}} - \boldsymbol{v}) &= \boldsymbol{K}_{m_1}\boldsymbol{v}_{tt}, \\ \boldsymbol{K}_{m_2}\bar{\boldsymbol{u}}_{tt} + \boldsymbol{K}_{v_2}(\bar{\boldsymbol{u}}_t - \boldsymbol{u}_t) + \boldsymbol{K}_{p_2}(\bar{\boldsymbol{u}} - \boldsymbol{u}) &= \boldsymbol{K}_{m_2}\boldsymbol{u}_{tt}. \end{aligned} \tag{17}$$

Defining the error vector $\boldsymbol{e}(t) = (\bar{\boldsymbol{v}} - \boldsymbol{v}, \bar{\boldsymbol{u}} - \boldsymbol{u})^T$ and writing (17) in terms of this error, the closed-loop system dynamics take the form of standard homogeneous second-order differential equations:

$$\boldsymbol{e}_{tt} + \boldsymbol{K'}_v\boldsymbol{e}_t + \boldsymbol{K'}_p\boldsymbol{e} = \boldsymbol{0}, \tag{18}$$

where the matrices $\boldsymbol{K'}_v$ and $\boldsymbol{K'}_p$ are defined as

$$\begin{aligned} \boldsymbol{K'}_v &= \begin{bmatrix} \boldsymbol{K}_{v_1} \oslash \boldsymbol{K}_{m_1} & 0 \\ 0 & \boldsymbol{K}_{v_2} \oslash \boldsymbol{K}_{m_2} \end{bmatrix}, \\ \boldsymbol{K'}_p &= \begin{bmatrix} \boldsymbol{K}_{p_1} \oslash \boldsymbol{K}_{m_1} & 0 \\ 0 & \boldsymbol{K}_{p_2} \oslash \boldsymbol{K}_{m_2} \end{bmatrix}, \end{aligned} \tag{19}$$

in which $\oslash$ denotes element-wise division of matrices (Hadamard division). The matrices $\boldsymbol{K'}_v$ and $\boldsymbol{K'}_p$ are symmetric and positive definite. To show that $\boldsymbol{e}(t) \rightarrow \boldsymbol{0}$ as $t \rightarrow \infty$, the following positive definite quadratic Lyapunov function is chosen,

$$V = \frac{1}{2}\boldsymbol{e}_t^T\boldsymbol{e}_t + \frac{1}{2}\boldsymbol{e}^T\boldsymbol{K'}_p\boldsymbol{e}, \tag{20}$$

which has the following time derivative:

$$\begin{aligned} V_t &= \frac{1}{2}\boldsymbol{e}_{tt}^T\boldsymbol{e}_t + \frac{1}{2}\boldsymbol{e}_t^T\boldsymbol{e}_{tt} + \frac{1}{2}\boldsymbol{e}_t^T\boldsymbol{K'}_p\boldsymbol{e} + \frac{1}{2}\boldsymbol{e}^T\boldsymbol{K'}_p\boldsymbol{e}_t \\ &= \frac{1}{2}(\boldsymbol{e}_{tt}^T + \boldsymbol{e}^T\boldsymbol{K'}_p)\boldsymbol{e}_t + \frac{1}{2}\boldsymbol{e}_t^T(\boldsymbol{e}_{tt} + \boldsymbol{K'}_p\boldsymbol{e}) \\ &= \frac{1}{2}(-\boldsymbol{e}_t^T\boldsymbol{K'}_v)\boldsymbol{e}_t + \frac{1}{2}\boldsymbol{e}_t^T(-\boldsymbol{K'}_v\boldsymbol{e}_t) = -\boldsymbol{e}_t^T\boldsymbol{K'}_v\boldsymbol{e}_t. \end{aligned} \tag{21}$$

Since $\boldsymbol{K'}_v$ is positive definite, V_t is a negative definite function. By applying Lyapunov's direct method to the closed-loop system dynamics, we can prove that $\boldsymbol{e}(t) \rightarrow \boldsymbol{0}$ as $t \rightarrow \infty$ and the system is globally asymptotically stable [39].

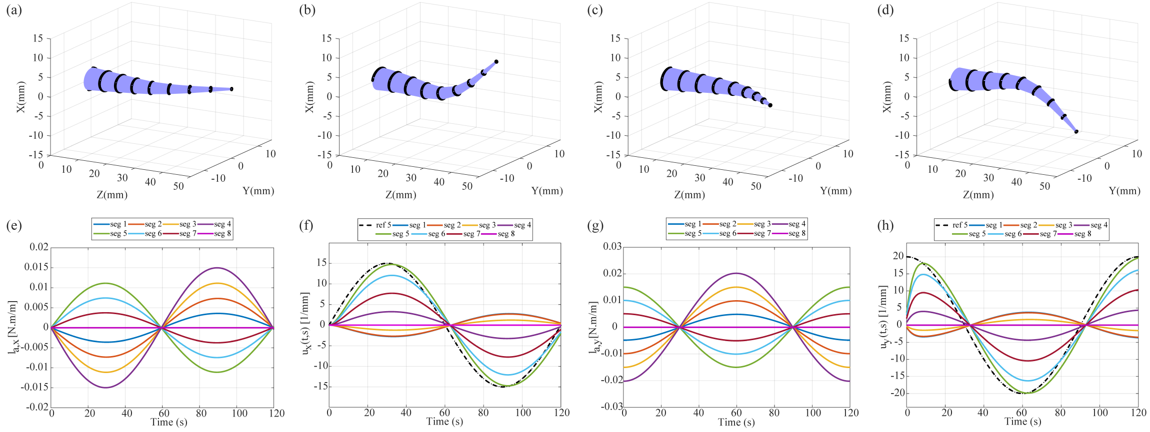

Fig. 2. Tracking performance for a reference configuration that requires bending deformations. (a)-(d) Simulation snapshots at times $t = 30\,s$, $60\,s$, $90\,s$, and $120\,s$, respectively. (e),(g) Applied moments about the x and y axes, respectively. (f),(h) Curvature components $\boldsymbol{u}_x$ and $\boldsymbol{u}_y$, respectively, of all segments, and the corresponding reference components $\bar{\boldsymbol{u}}_x$ and $\bar{\boldsymbol{u}}_y$ for segment 5. The average NRMSE over all spatial nodes is (f) 5.0%, (h) 5.3%.

IV. Simulation Results

In this section, the performance of the decentralized configuration tracking controller is validated with numerical simulations of a Cosserat rod model of the hydrogel-based segmented continuum robot arm in [9]. The simulated robot must achieve specified reference configurations through bending, torsion, shear, and extension. In all simulations, the relatively low values of the average normalized root-mean-square errors (NRMSEs) between the simulated and reference configurations over all spatial nodes (discretized locations along the robot's backbone) demonstrate effective tracking performance by the controller. These values are stated in figure captions in the following subsections.

As in our prior works on decentralized control of soft segmented continuum robots [36], [37], we assume that each segment of the robot has local sensing and actuation capabilities. For each test case, the simulated continuum robot arm is slender and symmetric about the z-axis, with isotropic material properties and the parameters listed in Table I.

Although the robot is simulated with circular cross-sections, our control approach can be applied to continuum robots with other cross-section geometries, as long as they satisfy the assumptions required for using the Cosserat rod model. Both uniform and tapered robot arms were simulated; the cross-section of the uniform arm has a constant radius r_p, while the radius of the cross-section of the tapered arm decreases from r_p at the proximal segment to r_d at the distal (tip) segment.

Since hydrogel has a slow response time, in practice, the control input frequencies must be low enough to give the material enough time to complete its heating and cooling phases. To demonstrate the applicability of our controller to other types of materials, we also simulated it on a robot arm composed of silicone, which has a faster response than hydrogel, with the parameters given in Table I. The dimensions L, r_p, and r_d of the simulated silicone robot arm were each 10 times longer than the corresponding dimensions of the hydrogel-based arm. The reference control inputs for the silicone arm were the same as the inputs defined for the hydrogel-based arm, except with amplitudes 10 times larger and, in the case of controlled shear deformations, a frequency 10 times smaller. The simulations of the silicone robot arm are presented in the supplementary video attachment.

For the arm made of hydrogel, which can only deform underwater, the applied force from the environment was defined as the gravitational force acting on the arm,

$$ {}^{G}\boldsymbol{f}_e = (\rho - \rho_w)A\boldsymbol{g} - {}^{G}\boldsymbol{R}\boldsymbol{C}\boldsymbol{q} \,\odot |\boldsymbol{q}|, \tag{22} $$

where ρ is the density of the hydrogel, ρ_w is the density of the surrounding water, $\boldsymbol{g}$ is gravitational acceleration, and $\boldsymbol{C}$ is the damping coefficient matrix of the arm, which is used to define the square-law drag force on the arm due to water resistance ($\odot$ denotes element-wise multiplication). The remaining forces and moments in (4) due to external loads and environmental effects were set to zero. For the arm made of silicone, which was assumed to operate in air, the density ρ in (22) was set to ρ_S, the density of silicone, and the drag force term was set to zero.

A. *Controlled Bending Deformations*

A tapered robot arm was simulated to track the following time-varying reference configuration, which requires bending deformations:

$$ \bar{\boldsymbol{u}}_x(t,s) = \begin{cases} 30\left(\dfrac{s}{L}\right)\sin(\omega t), & k = 1, ..., N/2 \\ 30\left(\dfrac{s-L}{L}\right)\sin(\omega t), & k = N/2+1, ..., N, \end{cases} \tag{23} $$

$$ \bar{\boldsymbol{u}}_y(t,s) = \begin{cases} 40\left(\dfrac{s}{L}\right)\cos(\omega t), & k = 1, ..., N/2 \\ 40\left(\dfrac{s-L}{L}\right)\cos(\omega t), & k = N/2+1, ..., N, \end{cases} \tag{24} $$

and $\bar{\boldsymbol{u}}_z(t,s) = 0$, where $\omega = 2\pi/120$ and $s = k \cdot ds$.

Figures 2a-d show snapshots of the simulated hydrogel-based arm over one cycle of the reference input. In these figures and in all subsequent simulation snapshots, only the

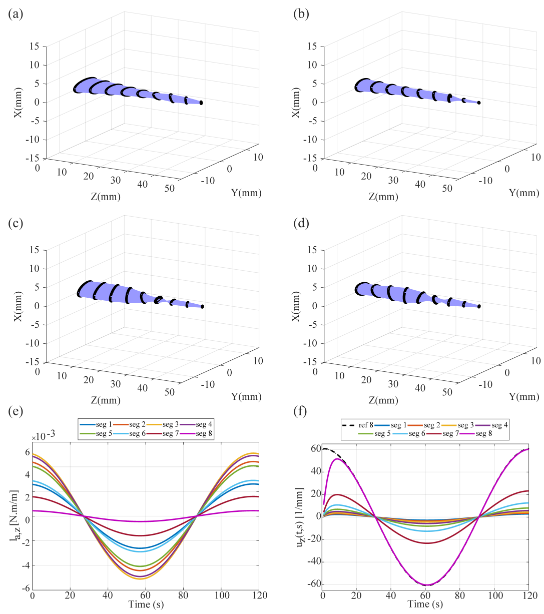

Fig. 3. Tracking performance for a reference configuration that requires torsion deformation. (a)-(d) Simulation snapshots at $t = 5\,s$, $15\,s$, $30\,s$, and $45\,s$, respectively. (e) Applied moments about the z axis. (f) Curvature components $\boldsymbol{u}_z$ for all segments and $\bar{\boldsymbol{u}}_z$ for segment 8. The average NRMSE over all spatial nodes is 4.54%.

$N_v = 8$ virtual segments (bounded by black rings on the arm), rather than all $N = 80$ spatial nodes, are displayed for clearer visualization. Each node traces out an ellipse in the $x-y$ plane while exhibiting bending deformations about lines in this plane. Figures 2e and 2g plot the time evolution of the moments applied by the actuators about the x and y axes. The segments' curvature vector components $\boldsymbol{u}_x$ and $\boldsymbol{u}_y$ are plotted over time in Figs. 2f and 2h, along with the reference components for segment 5. It is evident that $\boldsymbol{u}_x$ and $\boldsymbol{u}_y$ for this segment remain close to their reference profiles.

B. Controlled Torsion Deformations

Twisting motions about the z-axis of the robot arm can be simulated by applying a moment about this axis to each spatial node along the arm. We simulated torsion deformation in a tapered robot arm by applying the time-varying reference configuration

$$\bar{\boldsymbol{u}}_z(t,s) = 60\left(\frac{s}{L}\right)\cos(\omega t), \quad \omega = 2\pi/120, \tag{25}$$

and setting $\bar{\boldsymbol{u}}_x(t,s) = \bar{\boldsymbol{u}}_y(t,s) = 0$. Four snapshots of the simulated hydrogel-based arm over one cycle of the reference input are shown in Figs. 3a-d. Fig. 3e plots the time evolution of the moments applied by the actuators about the z axis in the local frame of each segment. The corresponding curvature vector components $\boldsymbol{u}_z$ are plotted in Fig. 3f and compared with the reference component for segment 8.

C. Controlled Shear Deformations

To our knowledge, shear deformation has not previously been simulated in soft robot arms, despite the development of models that are capable of describing shear in such structures [19]. We simulated shear deformation in robot arms with uniform cross-sectional areas. In these simulations, we

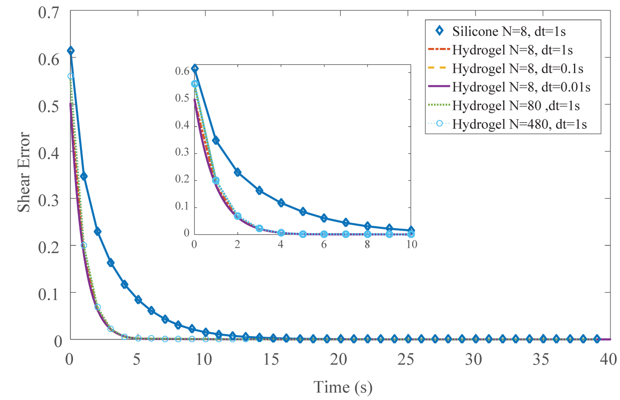

Fig. 4. Average $||\boldsymbol{e}(t)||_2$ over time of a simulated continuum robot arm undergoing shear deformation, with exponentially decaying reference inputs $\bar{\boldsymbol{v}}_x$ and $\bar{\boldsymbol{v}}_y$ for different values of N, dt, and ρ. The inset figure shows a close-up of the plots during the first $10\,s$.

defined reference shear components $\bar{\boldsymbol{v}}_x$ and $\bar{\boldsymbol{v}}_y$ whose values did not exceed the values of $\boldsymbol{v}_x$ and $\boldsymbol{v}_y$ produced during the bending simulation described in Section IV-A, to ensure that they did not exceed values that would result in material failure. Our definitions of these reference components are based on the kinematic locomotion of a burrowing worm simulated in one dimension [14] and the elongation motions that octopus arms exhibit when their transverse muscles contract [11], [13]. The reference components were defined as:

$$\bar{\boldsymbol{v}}_x(t,s) = \bar{\boldsymbol{v}}_y(t,s) = 4\sin\left(\omega\left(t - 1 + \frac{s}{L}\right)\right), \quad \omega = \frac{2\pi c}{\lambda}, \tag{26}$$

and $\bar{\boldsymbol{v}}_z(t,s) = 0$. In order to accurately simulate the shear deformations, the cross-sectional area of the arm must be updated at each time step of the simulation with the reference components as follows [14]:

$$A_i = A_0 / \sqrt{\bar{\boldsymbol{v}}_x{}^2 + \bar{\boldsymbol{v}}_y{}^2}, \quad i = 1, ..., N, \tag{27}$$

where A_0 is the initial cross-section area.

We simulated the responses of hydrogel-based and silicone robot arms to the reference components $\bar{\boldsymbol{v}}_x$ and $\bar{\boldsymbol{v}}_y$. For the hydrogel arm, we set the wave velocity to $c = 1/2\pi$ m/s and the wavelength to $\lambda = L$ m. With these parameters, each spatial node along the robot arm follows a sinusoidal trajectory with equal amplitudes in the x and y directions and a frequency of $\omega \approx 22$ Hz. This frequency was selected in order to visualize the traveling wave response of the robot arm over a short time period ($12\,s$), although in practice, it may be too high to be implemented in hydrogel material. In the silicone arm simulation, the reference input frequency was set to $\omega \approx 2$ Hz. Figures 5a-d plot snapshots of the simulated hydrogel arm over one cycle of the reference input. The forces applied by the actuators along the x and y axes are plotted over time in Figs. 5e and 5g, and the segments' components $\boldsymbol{v}_x$ and $\boldsymbol{v}_y$ and the reference values for segment 4 are plotted over time in Figs. 5f and 5h.

To study the effects of the number of spatial nodes N, the time step, dt, and the material density, ρ, on the controller

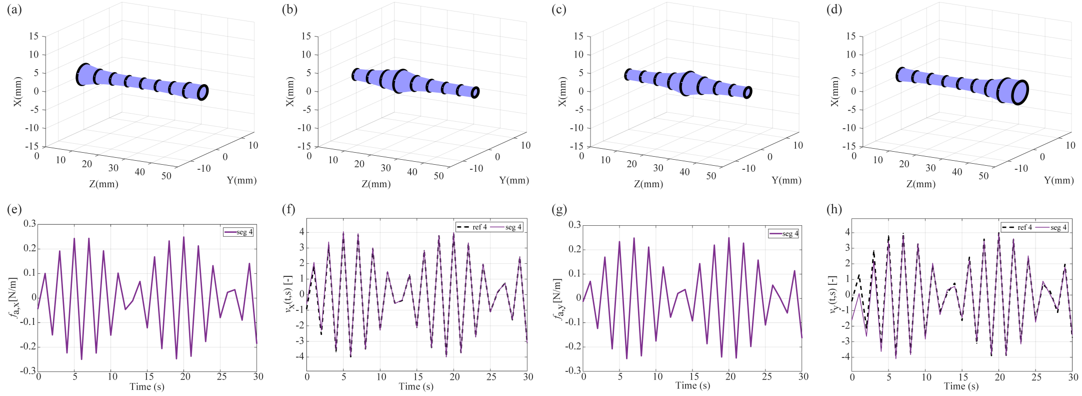

Fig. 5. Tracking performance for a reference configuration that requires shear deformations. (a)-(d) Simulation snapshots at $t = 1\,s$, $6\,s$, $8\,s$, and $12\,s$, respectively. (e),(g) Applied forces along the x and y axes, respectively. (f),(h) Components $\boldsymbol{v}_x$ and $\boldsymbol{v}_y$, respectively, for segment 4, and the reference components $\bar{\boldsymbol{v}}_x$ and $\bar{\boldsymbol{v}}_y$ for this segment. The average NRMSE over all spatial nodes is (f) 6.15%, (h) 6.3%.

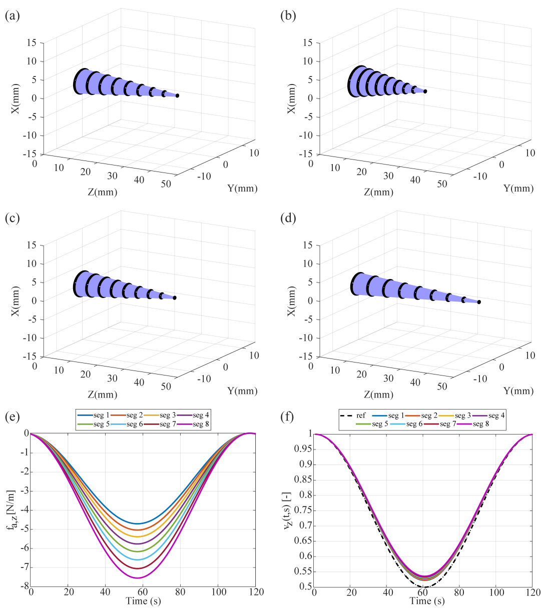

Fig. 6. Tracking performance for a reference configuration that requires extension deformations. (a)-(d) Simulation snapshots at $t = 30\,s$, $60\,s$, $90\,s$, and $120\,s$, respectively. (e) Applied forces along the z axis. (f) Components $\boldsymbol{v}_z$ and $\bar{\boldsymbol{v}}_z$ for all segments. Average NRMSE over all spatial nodes is 1.3%.

performance, shear deformations were simulated in both hydrogel and silicone robot arms for different combinations of N and dt values. For each case, the norm of the shear tracking error, $\boldsymbol{e}(t) = (\bar{\boldsymbol{v}} - \boldsymbol{v}, \boldsymbol{0})^T$, is plotted over time in Fig. 4. Although N and dt must be chosen carefully to avoid producing numerical instability, the results show that the numerical solution of the closed-loop dynamics remains stable over a wide range of N and dt values, without exhibiting a significant variation in performance. Therefore, we selected $dt = 0.1\,s$ and $N = 80$ to achieve acceptable model accuracy without excessive simulation times.

D. Controlled Extension Deformations

A continuum robot arm can extend and contract along its central axis if its material and design allow the cross-section of the arm to expand and shrink [16], [41]. These deformations are similar to those produced by muscular hydrostats such as octopus arms, which elongate or shorten by contracting their transverse or longitudinal muscles while maintaining a constant volume [11], [13]. We simulated extension and contraction in a tapered robot arm by applying the time-varying reference configuration

$$\bar{\boldsymbol{v}}_z(t,s) = 0.75 + 0.25\cos(\omega t)\,, \tag{28}$$

and setting $\bar{\boldsymbol{v}}_x(t,s) = \bar{\boldsymbol{v}}_y(t,s) = 0$. This reference input affects all spatial nodes equally with the same frequency, $\omega = 2\pi/120$ Hz. To enforce a constant volume during extension, mimicking the isovolumetric property of a muscular hydrostat, the cross-sectional area of the arm is updated at each time step of the simulation as $A_i = A_0/\bar{\boldsymbol{v}}_z$, $i = 1,...,N$ [14]. Figures 6a-d plot snapshots of the simulated hydrogel-based arm over one cycle of the reference input. Figure 6e plots the time evolution of the forces applied by the actuators along the z axis of the local frame of each segment, and Fig. 6f compares the segments' components $\boldsymbol{v}_z$ to the reference input $\bar{\boldsymbol{v}}_z$.

V. Conclusions and Future Work

We have presented a novel approach to dynamic control of bending, torsion, shear, and extension deformations in a soft continuum robot arm by applying an inverse dynamics controller combined with a decentralized controller that incorporates the system stiffness and damping in the gain matrices. This decentralized control approach can be implemented in a computationally efficient way on a continuum robot arm with independently-controllable actuators enabling it to perform dexterous motions in three dimensions, and it is robust to individual actuator failures. To our knowledge, this is the first control approach for soft continuum robot arms that achieves tracking of configurations which require shear deformations. We validate our controller in simulations of a segmented continuum robot arm that are based on the geometrically exact Cosserat rod model. Our test cases include simulations in which the actuators that apply forces and moments on the elastic rod have the physical properties of a hydrogel material used in our prior work [9]. In all simulated test cases, the controller produces average NRMSEs in configuration tracking below 7%, indicating effective tracking performance. The controller's performance is consistent over a wide range of values for the simulation parameters N and dt.

As future work, our plan is to validate the proposed inverse dynamics control approach and demonstrate controllers for object grasping tasks on a 3D version of the hydrogel-based robotic arm [9]. To implement the decentralized controller in practice, both local sensing and actuation are required, and there are possibilities for adding local sensing to the next version of our hydrogel-based continuum robot.

References

[1] D. Rus and M. T. Tolley, "Design, fabrication and control of soft robots," *Nature*, vol. 521, no. 7553, pp. 467–475, 2015.

[2] I. D. Walker, "Continuous backbone "continuum" robot manipulators," *International Scholarly Research Notices*, vol. 2013, 2013.

[3] R. J. Webster III and B. A. Jones, "Design and kinematic modeling of constant curvature continuum robots: A review," *The International Journal of Robotics Research*, vol. 29, no. 13, pp. 1661–1683, 2010.

[4] T. George Thuruthel, Y. Ansari, E. Falotico, and C. Laschi, "Control strategies for soft robotic manipulators: A survey," *Soft Robotics*, vol. 5, no. 2, pp. 149–163, 2018.

[5] D. Trivedi, A. Lotfi, and C. D. Rahn, "Geometrically exact models for soft robotic manipulators," *IEEE Transactions on Robotics*, vol. 24, no. 4, pp. 773–780, 2008.

[6] M. Cianchetti, A. Arienti, M. Follador, B. Mazzolai, P. Dario, and C. Laschi, "Design concept and validation of a robotic arm inspired by the octopus," *Materials Science and Engineering: C*, vol. 31, no. 6, pp. 1230–1239, 2011.

[7] I. S. Godage, G. A. Medrano-Cerda, D. T. Branson, E. Guglielmino, and D. G. Caldwell, "Dynamics for variable length multisection continuum arms," *The International Journal of Robotics Research*, vol. 35, no. 6, pp. 695–722, 2016.

[8] R. Khodambashi, Y. Alsaid, R. Rico, H. Marvi, M. M. Peet, R. E. Fisher, S. Berman, X. He, and D. M. Aukes, "Heterogeneous hydrogel structures with spatiotemporal reconfigurability using addressable and tunable voxels," *Advanced Materials*, p. 2005906, 2021.

[9] A. Doroudchi, R. Khodambashi, A. S. Lafmejani, D. M. Aukes, and S. Berman, "Dynamic modeling of a hydrogel-based continuum robotic arm with experimental validation," in *IEEE Int'l. Conference on Soft Robotics (RoboSoft)*, 2020, pp. 695–701.

[10] L. Bakule, "Decentralized control: An overview," *Annual Reviews in Control*, vol. 32, no. 1, pp. 87–98, 2008.

[11] S. Kolachalama and S. Lakshmanan, "Continuum robots for manipulation applications: A survey," *Journal of Robotics*, vol. 2020, 2020.

[12] S. M. R. Sorkhabadi, P. T. Chinimilli, D. Gaytan-Jenkins, and W. Zhang, "Human locomotion activity and speed recognition using electromyography based features," in *2019 Wearable Robotics Association Conference (WearRAcon)*, 2019, pp. 80–85.

[13] W. M. Kier and K. K. Smith, "Tongues, tentacles and trunks: the biomechanics of movement in muscular-hydrostats," *Zoological Journal of the Linnean Society*, vol. 83, no. 4, pp. 307–324, 1985.

[14] F. Boyer, S. Ali, and M. Porez, "Macrocontinuous dynamics for hyperredundant robots: application to kinematic locomotion bioinspired by elongated body animals," *IEEE Transactions on Robotics*, vol. 28, no. 2, pp. 303–317, 2011.

[15] L. Niu, L. Ding, H. Gao, Y. Su, Z. Deng, and Z. Liu, "Closed-form equations and experimental verification for soft robot arm based on Cosserat theory," in *IEEE/RSJ Int'l. Conference on Intelligent Robots and Systems (IROS)*, 2019, pp. 6630–6635.

[16] Q. Guan, J. Sun, Y. Liu, N. M. Wereley, and J. Leng, "Novel bending and helical extensile/contractile pneumatic artificial muscles inspired by elephant trunk," *Soft Robotics*, 2020.

[17] S. S. Antman, "Problems in nonlinear elasticity," *Nonlinear Problems of Elasticity*, pp. 513–584, 2005.

[18] J. Till, V. Aloi, and C. Rucker, "Real-time dynamics of soft and continuum robots based on Cosserat rod models," *The Int'l. Journal of Robotics Research*, vol. 38, no. 6, pp. 723–746, 2019.

[19] F. Renda, V. Cacucciolo, J. Dias, and L. Seneviratne, "Discrete Cosserat approach for soft robot dynamics: A new piece-wise constant strain model with torsion and shears," in *IEEE/RSJ Int'l. Conference on Intelligent Robots and Systems (IROS)*, 2016, pp. 5495–5502.

[20] B. Siciliano, L. Sciavicco, L. Villani, and G. Oriolo, *Robotics: modelling, planning and control*. Springer Science & Business Media, 2010.

[21] C. Della Santina, R. K. Katzschmann, A. Bicchi, and D. Rus, "Model-based dynamic feedback control of a planar soft robot: Trajectory tracking and interaction with the environment," *The International Journal of Robotics Research*, vol. 39, no. 4, pp. 490–513, 2020.

[22] A. Kapadia and I. D. Walker, "Task-space control of extensible continuum manipulators," in *IEEE/RSJ Int'l. Conference on Intelligent Robots and Systems (IROS)*, 2011, pp. 1087–1092.

[23] T. George Thuruthel, F. Renda, and F. Iida, "First-order dynamic modeling and control of soft robots," *Frontiers in Robotics and AI*, vol. 7, no. 95, 2020.

[24] C. Wang, C. G. Frazelle, J. R. Wagner, and I. Walker, "Dynamic control of multi-section three-dimensional continuum manipulators based on virtual discrete-jointed robot models," *IEEE/ASME Transactions on Mechatronics*, 2020.

[25] C. Duriez, "Control of elastic soft robots based on real-time finite element method," in *IEEE Int'l. Conference on Robotics and Automation (ICRA)*, 2013, pp. 3982–3987.

[26] R. K. Katzschmann, M. Thieffry, O. Goury, A. Kruszewski, T.-M. Guerra, C. Duriez, and D. Rus, "Dynamically closed-loop controlled soft robotic arm using a reduced order finite element model with state observer," in *IEEE Int'l. Conference on Soft Robotics (RoboSoft)*, 2019, pp. 717–724.

[27] N. Naughton, J. Sun, A. Tekinalp, G. Chowdhary, and M. Gazzola, "Elastica: A compliant mechanics environment for soft robotic control," *arXiv preprint arXiv:2009.08422*, 2020.

[28] H.-S. Chang, U. Halder, C.-H. Shih, A. Tekinalp, T. Parthasarathy, E. Gribkova, G. Chowdhary, R. Gillette, M. Gazzola, and P. G. Mehta, "Energy shaping control of a cyberoctopus soft arm," *arXiv preprint arXiv:2004.05747*, 2020.

[29] H.-S. Chang, U. Halder, E. Gribkova, A. Tekinalp, N. Naughton, M. Gazzola, and P. G. Mehta, "Controlling a cyberoctopus soft arm with muscle-like actuation," *arXiv preprint arXiv:2010.03368*, 2020.

[30] J. Stoer and R. Bulirsch, *Introduction to numerical analysis*. Springer Science & Business Media, 2013, vol. 12.

[31] M. Schaller, S. M. R. Sorkhabadi, and W. Zhang, "Robotic shoe: An ankle assistive device for gait plantar flexion assistance," in *2020 Design of Medical Devices Conference*. American Society of Mechanical Engineers Digital Collection, 2019.

[32] P. T. Chinimilli, S. M. R. Sorkhabadi, and W. Zhang, "Assessment of human dynamic gait stability with a lower extremity assistive device," *IEEE Transactions on Neural Systems and Rehabilitation Engineering*, vol. 28, no. 3, pp. 669–678, 2020.

[33] R. W. Holsapple, "A modified simple shooting method for solving two-point boundary value problems," Ph.D. dissertation, Texas Tech University, 2003.

[34] J. Till and D. C. Rucker, "Elastic rod dynamics: Validation of a real-time implicit approach," in *IEEE/RSJ Int'l. Conference on Intelligent Robots and Systems (IROS)*, 2017, pp. 3013–3019.

[35] J. Linn, H. Lang, and A. Tuganov, "Geometrically exact Cosserat rods with Kelvin–Voigt type viscous damping," *Mechanical Sciences*, vol. 4, no. 1, pp. 79–96, 2013.

[36] A. Doroudchi, S. Shivakumar, R. E. Fisher, H. Marvi, D. Aukes, X. He, S. Berman, and M. M. Peet, "Decentralized control of distributed actuation in a segmented soft robot arm," in *IEEE Conference on Decision and Control (CDC)*, 2018, pp. 7002–7009.

[37] A. S. Lafmejani, H. Farivarnejad, A. Doroudchi, and S. Berman, "A consensus strategy for decentralized kinematic control of multi-segment soft continuum robots," in *American Control Conference (ACC)*, 2020, pp. 909–916.

[38] A. S. Lafmejani, A. Doroudchi, H. Farivarnejad, X. He, D. Aukes, M. M. Peet, H. Marvi, R. E. Fisher, and S. Berman, "Kinematic modeling and trajectory tracking control of an octopus-inspired hyper-redundant robot," *IEEE Robotics and Automation Letters*, vol. 5, no. 2, pp. 3460–3467, 2020.

[39] H. K. Khalil and J. W. Grizzle, *Nonlinear systems*. Prentice Hall Upper Saddle River, NJ, 2002, vol. 3.

[40] R. Khodambashi, Y. Alsaid, D. Aukes, and X. He, "Shape Morphing Soft Material," 2019, US Provisional Patent 62/860,700.

[41] T. Morales Bieze, A. Kruszewski, B. Carrez, and C. Duriez, "Design, implementation, and control of a deformable manipulator robot based on a compliant spine," *The International Journal of Robotics Research*, vol. 39, no. 14, pp. 1604–1619, 2020.